



**HAL**  
open science

# A hybrid sub-structuring method for prediction of air inlet sound transmission

J. Puig, Mathieu Aucejo, J.-F. Deü, Walid Larbi, P. Macquart

► **To cite this version:**

J. Puig, Mathieu Aucejo, J.-F. Deü, Walid Larbi, P. Macquart. A hybrid sub-structuring method for prediction of air inlet sound transmission. *Journal of Sound and Vibration*, 2024, 569, pp.117994. 10.1016/j.jsv.2023.117994 . hal-04181997

**HAL Id: hal-04181997**

**<https://hal.science/hal-04181997>**

Submitted on 16 Aug 2023

**HAL** is a multi-disciplinary open access archive for the deposit and dissemination of scientific research documents, whether they are published or not. The documents may come from teaching and research institutions in France or abroad, or from public or private research centers.

L'archive ouverte pluridisciplinaire **HAL**, est destinée au dépôt et à la diffusion de documents scientifiques de niveau recherche, publiés ou non, émanant des établissements d'enseignement et de recherche français ou étrangers, des laboratoires publics ou privés.

# A hybrid sub-structuring method for prediction of air inlet sound transmission

J. Puig, M. Aucejo, J.-F. Deü and W. Larbi<sup>a</sup>, P. Macquart<sup>b</sup>

<sup>a</sup>*Laboratoire de Mécanique des Structures et des Systèmes Couplés (LMSSC),  
Conservatoire National des Arts et Métiers (Cnam), HESAM Université, 292 rue  
Saint-Martin, 75003, Paris, France*

<sup>b</sup>*Union des Fabricants de Menuiseries (UFME), 39 rue Louis Blanc, 92038 Courbevoie.  
France*

---

## Abstract

Air inlets coupled with mechanically controlled ventilation systems are widely used to renew polluted indoor air. They are generally positioned at the top of windows inducing a reduction of the sound insulation. As the harmful consequences of noisy environments on human health are more and more highlighted, it becomes necessary to maximize the sound insulation while ensuring a sufficient fresh air flow. To this end, efficient numerical simulation appears to be a promising way for studying air inlet acoustic behavior: many parameters can be considered without the need to carry out costly and time-consuming laboratory tests. This work aims at developing a reliable numerical model reproducing the acoustic laboratories used by manufacturers for the measurements of air inlet sound reduction index. The low frequency range is studied in the present paper as the measurement uncertainties arising from experimental conditions are the greatest at these frequencies. In order to make the calculations computationally efficient, the proposed model

---

\*Corresponding author. E-mail address: mathieu.aucejo@lecnam.net

uses a sub-structuring approach called the Patch Transfer Function (PTF) method, and combines analytical or numerical solutions, depending on the subdomain considered. Each subsystem of complex geometries is discretized using finite elements. Conversely, the PTF of simple geometries are analytically computed from a modal decomposition, enriched with a quasi-static correction numerically computed. As empirical improvements pointed out the benefits of the addition of melamine foams, porous material modelling is introduced in the study based on an equivalent fluid model.

*Keywords:* Air inlets, Patch Transfer Function Method, Noise reduction, Porous materials, Quasi-static correction

---

## 1. Introduction

The consequences of noise pollution on health, economy and productivity are increasingly acknowledged. The European Environment Agency estimates that over 100 million people in Europe are exposed to harmful levels of environmental noise pollution, mainly from their homes, inducing huge social costs [1]. Thus, reduction of noise has become a key issue in most industrial fields, especially in the building industry. Factually, windows remain the primary entry point for external noise as their soundproofing is drastically reduced by the installation of air-inlets, made mandatory to provide ventilation in homes. In order to quantify the acoustic performance of their products, manufacturers measure a SRI (Sound Reduction Index) called  $D_{n,e}$  in acoustic laboratories [2]. This indicator shows the acoustic absorption in third octave bands from 100Hz to 5000Hz. However, manufacturers usually provide customers with a single value to characterize the acoustic absorption

of their products over the entire frequency range, the  $D_{n,e,w}$  [3].

However, it is known that the experimental conditions of air inlet testing imply a degree of uncertainty in measurements. Lots of studies pointed out that dispersion on the measured SRI arise when low frequencies are involved. The influence of laboratory properties and mounting conditions on the measurements was pointed out in Ref. [4]. Later, it was shown in Ref. [5] that the acoustic field in the low frequency range is dominated by normal modes, so the hypothesis of a diffuse field cannot be validated. In addition, an increase of uncertainties is demonstrated in Ref. [6] when low frequencies are taken into account for the calculation of a single absorption value. Many other studies emphasize that uncertainties increase when low frequencies are involved and mention the need to assess them [7–9]. As a result, factors such as the size of the room, the position and orientation of the loudspeakers and microphones as well as the mounting system potentially reduce the accuracy of the measurements, making air inlet testing difficult to replicate and reproduce.

This highlights the need for a numerical tool dedicated to the prediction of the acoustic performances of a window air inlet. It turns out that the noise transmission of windows and building facades have been more widely modelled [10, 11] than that of air inlets. Several studies deal with the acoustics of ventilation windows and investigate different ways to increase the transmission loss factor, as the use of porous materials, perforated panels, resonators or active noise attenuation systems [12, 13]. Closer to our issue, Jean et al. estimated the  $D_{n,e}$  of a simple rectangular wall air inlet, potentially covered

with absorbing materials [14, 15]. A previous study by the authors was dedicated to the calculation of the Transmission Loss (TL) of a single air-inlet using the Finite Element Method (FEM) [16]. This study highlights the need to model the rooms coupled to the air inlet in order to directly estimate its sound transmission. So, the main goal of this research is the development of a reliable model for the prediction of the noise transmission of air-inlets, while taking the complexity of their geometries, the coupling with the testing rooms and the presence of porous materials into account.

The large frequency range considered in the tests (50-5000 Hz) and the need to integrate the testing rooms in the model make it difficult to choose the appropriate method. At low frequencies, the reliability of the Finite Element Method (FEM) has been widely demonstrated since its early developments [17] for various applications including porous material modelling [18], which have a significant role in noise absorption of air inlets. The Boundary Element Method (BEM) is an alternative to the FEM where only the boundaries are discretized [19]. This powerful method shows great results for radiation problems in infinite space (among others) but is less appropriate for our study, as the inside of the air inlet has to be precisely modelled. Also, prediction of sound absorption and transmission of multi-layered materials is commonly studied with the Transfer Matrix Method (TMM) [20]. The method can take into account porous media, allowing to define a local impedance for the dissipative interfaces [21]. So, computationally efficient FEM-TMM models have been developed (FEM for the fluid, TMM for the porous media) with the added benefit of taking into account finite size effects and lateral boundary conditions [22]. In addition, in linear acoustics,

as the system can be described by partial derivative equations and boundary conditions, the pressure field in the domain can be calculated from a modal expansion [23]. As the testing rooms are far too large to be considered with FEM, analytical modal decomposition seems to be an interesting way to consider them, provided that their geometries are simple enough.

Despite their reliability and precision, the previously mentioned methods (except for the TMM) are overwhelmed in high frequencies because of the quantity of information required [24]. For FEM and BEM, increasing the frequency amounts to decrease the element size, leading to a huge number of degrees of freedom and prohibitive calculation time. Similarly, modes of a system are easy to calculate and well separated at low frequencies, but they start to overlap and multiply at high frequencies or for large geometries, making the modal approach less relevant. Moreover, all the previously described methods are deterministic and thus require a rigorous knowledge of the geometries, the assemblies, the parameters of materials, the nature of sources, etc. These elements led to the development of other acoustic methods dedicated to the high frequency range. For example, statistical approaches are based on the energy transfer between subsystems (Statistical Energy Analysis [24, 25], Wave Intensity Analysis [26], Power Flow method [27], etc). Also, high frequency analysis can be done using ray-tracing [28].

This paper focuses on the study of geometrical and material parameters in the low frequency range (50-1000 Hz) and their influence on the sound transmission of air inlets. As the problem involves a small air inlet coupled with two large testing rooms, a full Finite Element model is too time-

consuming. Therefore, the Patch Transfer Function method is used [29–32], which involves separate calculations on the uncoupled subsystems before re-assembling them from the continuity of normal velocity and pressure at the interfaces. In this paper, Finite Element method is used for the air inlet, while a semi-analytical modal summation is used for the rectangular testing rooms. To reduce the truncation error caused by the stiffness contribution of the modes outside the bandwidth of interest, convergence acceleration of the PTF of the rooms is necessary. Several methods, based on the estimation of residual mode contributions [31, 33], exist to address this issue. Our approach is based on these methods: a FE calculation is used at a single frequency in the rooms to evaluate contributions of higher modes. This approach leads to a hybrid evaluation of the PTF, which is one of the originalities of the present contribution.

The paper is organized as follows; Section 2 defines more precisely the acoustic indicators involved, recalls the results of a previously developed FEM model of a single air inlet and explains the need to consider the testing rooms using a sub structuring method. Section 3 covers the principles of the PTF approach and validates its implementation on simple geometries including porous materials. Section 4 deals with convergence acceleration for the PTF of the testing rooms is carried out in. Then, Section 5 applies the PTF method on a real geometry of air inlet coupled with reduced testing rooms.

## 2. Acoustic indicators and industrial issue

The experimental set-up for the measurement of air inlets sound absorption is shown in Fig. 1 and has to meet standard ISO 10140 [2]. Two coupled rigid-walled rooms are connected by an opening in which the tested air inlet can be installed. A loudspeaker emits a white noise in the emission room and the mean sound pressure level is measured in both rooms by a set of microphones. From these measurements, the  $D_{n,e}$  is defined as:

$$D_{n,e} = Lp_e - Lp_r + 10 \log_{10} \left( \frac{A_0}{A} \right), \quad (1)$$

with  $Lp_e$  and  $Lp_r$  the mean sound pressure level of the emission and reception room respectively,  $A_0$  the reference area fixed to  $10\text{m}^2$  and  $A$  the equivalent absorbing area of the reception room calculated with Sabine formula [2].

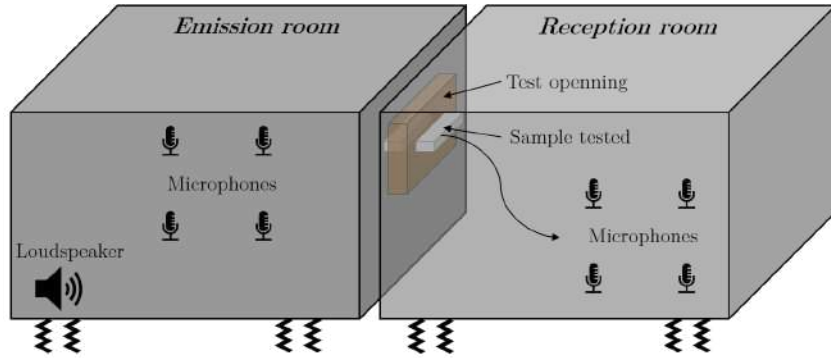


Figure 1: Experimental configuration for the measurement of the sound reduction index

As explained in section 1, manufacturers use the  $D_{n,e}$  to determine the  $D_{n,e,w}$ , a single value quantifying the general acoustic performance of their products. Two other single value indicators  $C$  and  $C_{tr}$  are often added, reflecting the acoustic insulation for two different types of noise source (low

and high frequencies) [3]. It is widely observed that testing rooms influence the measurements, particularly at low frequency: the modal density decreases and diffuse pressure field hypothesis is no longer verified. That is why the use of a FE model to compute the TL of a single air inlet, as made in Ref. [16] is not sufficient for  $D_{n,e}$  prediction, as the coupling with testing rooms is not taken into account.

Consequently, prediction of  $D_{n,e}$  means including testing rooms in the model as well as calculation of the sound pressure level (SPL) at several points in these rooms to get  $Lp_e$  and  $Lp_r$ . The size of the rooms would induce prohibitive calculation costs if they were modelled with FEM. Therefore a sub-structuring method called Patch Transfer Function is used to separate the calculation of the rooms from that of the air inlet [29, 31, 32]. The principles and interests of the method are explained in the next section, followed by a validation of SPL calculation at listening points on simple and complex geometries containing acoustic melamine. Special attention will be paid to gains in computation time made possible by the approach followed.

### 3. Patch Transfer Function Method

The Patch Transfer Function method is a sub-structuring approach for studying complex acoustic problems. It consists in the separation of the complete domain we need to resolve in several subdomains computed separately, before being assembled. To achieve this, the coupling surfaces between each subdomain are divided into elementary areas called patches. Transfer functions are then calculated between the patches and the possible sources and listening points in each uncoupled system. Then, the subdomains can be

assembled using continuity of the pressure and the normal velocity on each patch of the coupling surfaces. Thus, a PTF system is obtained having the normal velocity on the patches for unknown. Once the system is solved, the superposition principle is used to calculate the acoustic pressure at any listening point of the global domain, as the sum of each patch contribution [29, 32].

Lots of advantages result from this kind of approach. Firstly, each subdomain is calculated with the best fitted method. In the industrial case presented below, the simple geometries are computed using an analytical modal decomposition, while the complex geometries are solved using FEM. Note that the PTF of subsystems could also be obtained from experiments as done in Ref. [34]. Secondly, in the case where two neighboring meshed domains are considered, another advantage is that the meshes do not necessarily need to be compatible as physical quantities are averaged over the patches placed on the interface. Thirdly, if a subdomain is unchanged for several configurations, there is no need to calculate the transfer function again: only the PTF of the changing subdomains have to be recalculated or remeasured. Therefore, calculation costs are drastically reduced, notably for configurations where only a little part of the global domain is changing. Thus, the PTF approach could be a great help for the implementation of an optimization process of air inlets, as the testing rooms remain the same when the sample is changed.

In this section, the equations of the method are reminded and applied on the geometry shown in Fig. 2 which consists in two rigid-walled acoustic

rooms coupled with a simplified air inlet of rectangular shape.

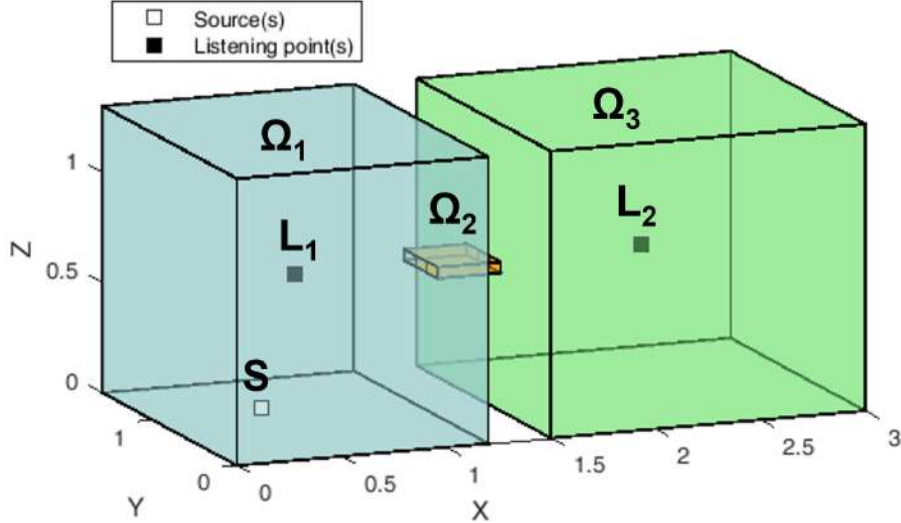


Figure 2: Description of the geometry. Three domains are separated by two interfaces, each discretized into three patches. Two listening points are placed in the subdomains  $\Omega_1$  and  $\Omega_3$ .

### 3.1. Description of the method

The complete domain  $\Omega$  is divided into three subdomains  $\Omega_1$ ,  $\Omega_2$  and  $\Omega_3$ . There are two coupling surfaces with  $N_1$  and  $N_2$  patches. An acoustic point source  $S$  is placed in  $\Omega_1$ . Two listening points are also considered:  $L_1$  placed in  $\Omega_1$  and  $L_2$  placed in  $\Omega_3$ .

The first step consists in calculating separately the transfer functions of each subdomain. Mathematically, a transfer function is the linear relation between the input and the output of an invariant system. For the PTF method, a pressure output caused by a normal velocity input is computed,

so the transfer function has the same meaning as an acoustic impedance. Here, the input/output entity can be a patch, a source or a listening point.

For an acoustic cavity  $\Omega_k$ , we define the PTF  $Z_{ij}^{\Omega_k}$  between an excited patch  $j$  and a receiver patch  $i$ , as the ratio of the averaged pressure  $\bar{p}_i^{\Omega_k}$  on the patch  $i$  and the averaged normal velocity  $\bar{v}_j^{\Omega_k}$  on the patch  $j$ :

$$Z_{ij}^{\Omega_k} = \frac{\bar{p}_i^{\Omega_k}}{\bar{v}_j^{\Omega_k}}, \quad (2)$$

where  $\bar{\bullet}_p = \frac{1}{S_p} \int_{S_p} \bullet dS_p$  is the space average on the patch  $p$  of surface  $S_p$ .

Likewise, on acoustic cavity  $\Omega_k$ , the PTF  $Z_{Lj}^{\Omega_k}$  is the ratio of the pressure  $p_L^{\Omega_k}$  on a listening point L and the average normal velocity  $\bar{v}_j^{\Omega_k}$  on the patch  $j$ :

$$Z_{Lj}^{\Omega_k} = \frac{p_L^{\Omega_k}}{\bar{v}_j^{\Omega_k}}. \quad (3)$$

With these definitions, the space averaged pressure  $\bar{p}_i^{\Omega_k}$  on a patch  $i$  of each uncoupled system is exclusively related to the velocity  $\bar{v}_j^{\Omega_k}$  of all patches  $j$  and a possible source term  $\tilde{p}_i^{\Omega_k}$  if there is a source in the cavity  $\Omega_k$ . In the example presented in Fig. 2, there is only one source, placed in  $\Omega_1$ , so the source term will be null for the two other cavities. In the end, pressure can be expressed as follows:

$$\bar{p}_i^{\Omega_k} = \tilde{p}_i^{\Omega_k} + Z_{ij}^{\Omega_k} \bar{v}_j^{\Omega_k}. \quad (4)$$

The previous equation is general and does not consider the interfaces. In order to specify it and then apply it to the acoustic problem presented in Fig. 2, we define the vector  $\bar{\mathbf{p}}_a^{\Omega_k}$  which contains the averaged pressure of all

the patches of the coupling surface  $a$  in the cavity  $\Omega_k$ . Likewise, we define the vector  $\bar{\mathbf{v}}_a^{\Omega_k}$  which contains the averaged normal velocity of all the patches of the coupling surface  $a$  in the cavity  $\Omega_k$ . Then, the pressure on the patches can be expressed in the three uncoupled domains as:

$$\left\{ \begin{array}{l} \bar{\mathbf{p}}_1^{\Omega_1} = \tilde{\mathbf{p}}_1^{\Omega_1} + \mathbf{Z}_{11}^{\Omega_1} \bar{\mathbf{v}}_1^{\Omega_1} \quad / \Omega_1 \\ \left[ \begin{array}{c} \bar{\mathbf{p}}_1^{\Omega_2} \\ \bar{\mathbf{p}}_2^{\Omega_2} \end{array} \right] = \left[ \begin{array}{cc} \mathbf{Z}_{11}^{\Omega_2} & \mathbf{Z}_{12}^{\Omega_2} \\ \mathbf{Z}_{21}^{\Omega_2} & \mathbf{Z}_{22}^{\Omega_2} \end{array} \right] \left[ \begin{array}{c} \bar{\mathbf{v}}_1^{\Omega_2} \\ \bar{\mathbf{v}}_2^{\Omega_2} \end{array} \right] \quad / \Omega_2 . \\ \bar{\mathbf{p}}_2^{\Omega_3} = \mathbf{Z}_{22}^{\Omega_3} \bar{\mathbf{v}}_2^{\Omega_3} \quad / \Omega_3 \end{array} \right. \quad (5)$$

Note that the subdomain  $\Omega_2$  involves two interfaces. Thus, the PTF matrix has diagonal and coupling terms.  $\mathbf{Z}_{mn}^{\Omega_k}$  represents the averaged pressure of the patches of the interface  $m$  caused by a unit average velocity of the patches of the interface  $n$ , in the subdomain  $\Omega_k$ .

Then, the coupling of the subdomains  $\Omega_1$ ,  $\Omega_2$  and  $\Omega_3$  is based on the continuity of the pressure and the normal velocity on each patch of the coupling surfaces. In the example described in this section, coupling conditions are:

$$\left\{ \begin{array}{l} \bar{\mathbf{p}}_1^{\Omega_1} = \bar{\mathbf{p}}_1^{\Omega_2} = \bar{\mathbf{p}}_1 \\ \bar{\mathbf{p}}_2^{\Omega_2} = \bar{\mathbf{p}}_2^{\Omega_3} = \bar{\mathbf{p}}_2 \\ \bar{\mathbf{v}}_1^{\Omega_1} = -\bar{\mathbf{v}}_1^{\Omega_2} = \bar{\mathbf{v}}_1 \\ \bar{\mathbf{v}}_2^{\Omega_2} = -\bar{\mathbf{v}}_2^{\Omega_3} = \bar{\mathbf{v}}_2 \end{array} \right. . \quad (6)$$

So, the system of Eq. (5) can be written:

$$\left[ \begin{array}{cc} \mathbf{Z}_{11}^{\Omega_1} + \mathbf{Z}_{11}^{\Omega_2} & \mathbf{Z}_{12}^{\Omega_2} \\ \mathbf{Z}_{21}^{\Omega_2} & \mathbf{Z}_{22}^{\Omega_2} + \mathbf{Z}_{22}^{\Omega_3} \end{array} \right] \left[ \begin{array}{c} \bar{\mathbf{v}}_1 \\ \bar{\mathbf{v}}_2 \end{array} \right] = \left[ \begin{array}{c} -\tilde{\mathbf{p}}_1^{\Omega_1} \\ 0 \end{array} \right]. \quad (7)$$

Here, dimensions of matrices  $\mathbf{Z}_{11}^{\Omega_1}$  and  $\mathbf{Z}_{11}^{\Omega_2}$  are  $N_1 \times N_1$ ,  $\mathbf{Z}_{12}^{\Omega_2}$  is  $N_1 \times N_2$ ,  $\mathbf{Z}_{21}^{\Omega_2}$  is  $N_2 \times N_1$ ,  $\mathbf{Z}_{22}^{\Omega_2}$  and  $\mathbf{Z}_{22}^{\Omega_3}$  are  $N_2 \times N_2$ .

The previous system can be expressed in a more compact form as:

$$\mathbf{Z}_\Omega \bar{\mathbf{v}} = -\tilde{\mathbf{p}}. \quad (8)$$

where  $\mathbf{Z}_\Omega$  is the PTF matrix of the global system and  $\tilde{\mathbf{p}}$  the source term. The vector  $\bar{\mathbf{v}}$  can then be deduced:

$$\bar{\mathbf{v}} = -\mathbf{Z}_\Omega^{-1} \tilde{\mathbf{p}}. \quad (9)$$

Finally, the pressure at the listening points can be calculated as a sum of the contribution of each patch and that of an eventual source  $\tilde{\mathbf{p}}_L^{\Omega_k}$  if a listening point  $L$  and a source are in the same subdomain  $\Omega_k$ :

$$\begin{cases} \mathbf{p}_L^{\Omega_1} = \tilde{\mathbf{p}}_L^{\Omega_1} + \mathbf{Z}_{L1}^{\Omega_1} \bar{\mathbf{v}}_1 \\ \mathbf{p}_L^{\Omega_3} = \mathbf{Z}_{L2}^{\Omega_3} \bar{\mathbf{v}}_2 \end{cases}, \quad (10)$$

with the PTF matrix  $\mathbf{Z}_{Li}^{\Omega_k}$  representing the pressure at the listening points  $L$  caused by the patch of the interface  $i$ , in the subdomain  $\Omega_k$ .

A validation of the method on several geometries is completed in the following section.

### 3.2. Validation of the PTF method

We present a validation of the PTF method applied on three configurations, one of them including porous materials. Modal and patches mesh convergences will be discussed, as well as the influence of the listening point

position on the accuracy of the results. Then, the calculation time of the PTF method will be compared to that of the FEM. Fig. 3 shows the geometries considered.

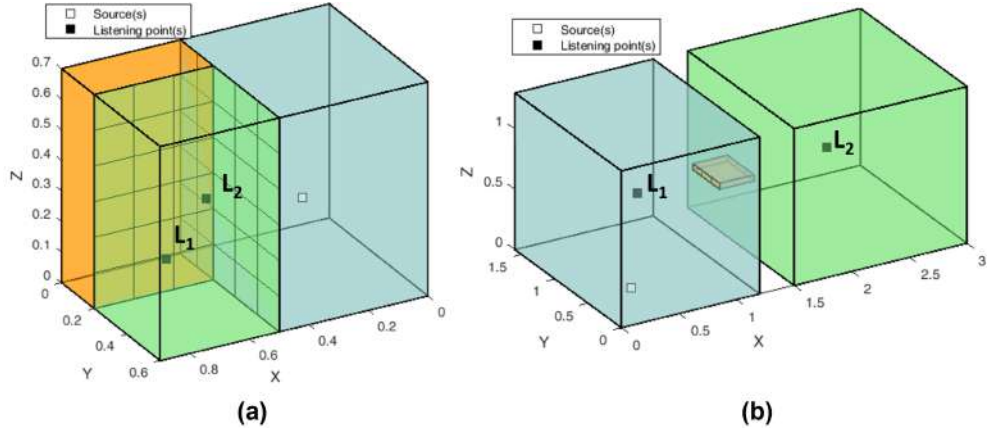


Figure 3: Geometries for PTF method validation. (a): first configuration with two listening points placed close and far from the interface, with all the sub domains filled with air. (b): second configuration (with all the sub domains filled with air) and third configuration (with the central sub domain filled with acoustic melamine)

### 3.2.1. First configuration

The first geometry consists in a rigid walled rectangular bloc filled with air divided into three subdomains, with one source and one listening point (see Fig. 3a). The SPL computed at the listening point using the PTF method is compared to a FEM reference computed in the whole domain. Table 1 gives all the geometrical parameters. Reference values at 15°C are taken for the air density  $\rho$  and the sound speed  $c$ . A general viscous fluid model is used, with a damping coefficient  $\eta$  which adds an imaginary part on the sound speed

and air density [35]:

$$\begin{cases} c_{eq} = c\sqrt{\left(1 + i\omega\frac{\eta}{c^2}\right)} \\ \rho_{eq} = \frac{\rho c^2}{c_{eq}^2} \end{cases} . \quad (11)$$

Table 1: Geometrical and physical parameters of the first system presented on Fig. 3. All lengths are in meters.

	$\Omega_1$	$\Omega_2$	$\Omega_3$
$(x ; y ; z)$	(0 ; 0 ; 0)	(0.5 ; 0 ; 0)	(0.5 ; 0.2 ; 0)
$(L_x ; L_y ; L_z)$	(0.5 ; 0.6 ; 0.7)	(0.4 ; 0.2 ; 0.7)	(0.4 ; 0.4 ; 0.7)
Source S	(0.2 ; 0.2 ; 0.2)		
Listening points	$L_1$ : (0.55 ; 0.25 ; 0.3), $L_2$ : (0.85 ; 0.55 ; 0.3)		
$\rho$	1.225 kg.m <sup>-3</sup>		
$c$	340.27 m.s <sup>-1</sup>		
$\eta$	0.02		

In a rigid acoustic cavity, the pressure  $P$  at a listening point  $L$  generated by a monopole source located at point  $S$  of amplitude  $Q(\omega)$  pulsating at the angular frequency  $\omega$  can be analytically calculated as an infinite sum of modal contributions [32]:

$$p(L, S, \omega) = Q(\omega) \sum_{k=1}^{\infty} \frac{\phi_k^L \phi_k^S}{(k_{eq}^2 - k_k^2) \Lambda_k}, \quad (12)$$

where  $\phi_k^L$ ,  $\phi_k^S$ ,  $k_{eq} = \frac{\omega}{c_{eq}}$ ,  $k_k = \frac{\omega_k}{c}$  and  $\Lambda_k$  are respectively, the mode shape evaluated at the point  $L$ , the modal shape evaluated at the point  $S$ , the wave number, the modal wave number and the modal mass of the mode  $k$ . We

remind that the mode shape  $\phi_{mnp}^P$  of mode of indices  $(m, n, p)$  at a point  $P$  of coordinates  $(x, y, z)$  in a rectangular box (dimensions  $L_x \times L_y \times L_z$ ) is given by:

$$\phi_{mnp}^P = \cos\left(\frac{m\pi}{L_x}x\right) \cos\left(\frac{n\pi}{L_y}y\right) \cos\left(\frac{p\pi}{L_z}z\right). \quad (13)$$

Similarly, each term of the analytical PTF matrices can be expressed as follows:

$$\begin{cases} Z_{ij}(\omega) = i\omega\rho_{eq}\Gamma_j \sum_{k=1}^M \frac{\langle\phi_k^i\rangle\langle\phi_k^j\rangle}{(k_{eq}^2 - k_k^2)\Lambda_k} \\ Z_{Lj}(\omega) = i\omega\rho_{eq}\Gamma_j \sum_{k=1}^M \frac{\phi_k^L\langle\phi_k^j\rangle}{(k_{eq}^2 - k_k^2)\Lambda_k} \end{cases}, \quad (14)$$

where  $\Gamma_j$  is the area of the patch  $j$  and  $\langle\phi_k^i\rangle$  is the mode shape (Eq. (13)) averaged on the patch  $i$ :

$$\langle\phi_k^i\rangle = \frac{1}{S_i} \int_{M \in S_i} \phi_k(M) dS_i. \quad (15)$$

The parameter  $n_{f_{max}}$  is introduced, linking  $f_{mode}$  the limiting frequency of the modal basis with  $f_{max}$  the maximum frequency of the study:

$$f_{mode} = n_{f_{max}} f_{max} \quad (16)$$

For instance, if  $n_{f_{max}} = 3$  and the maximum frequency of the study is 1kHz, all the modes having a natural frequency below 3kHz are kept in the modal basis. So the number of modes  $M$  retained in the modal basis depends on the parameter  $n_{f_{max}}$ .

The PTF approach implies to design patches on the interfaces. We define the criterion  $h$  as the ratio between the minimum wavelength  $\lambda_{min}$  and  $L$  the patch length. If  $h$  is set to 3 then they are at least 3 patches for one wavelength. So, this criterion has to be optimized.

For all the calculations, the accuracy of the PTF method is measured using the mean absolute error value:

$$e = \langle |\mathbf{Lp}_{PTF} - \mathbf{Lp}_{FEM}| \rangle, \quad (17)$$

with  $\mathbf{Lp}_{PTF}$  and  $\mathbf{Lp}_{FEM}$  respectively the SPL (the pressure reference for the calculation in dB is 20  $\mu\text{Pa}$ ) computed with the PTF approach and the FEM reference solution. All FEM models in this paper are meshed in 3D with 10 nodes tetrahedral elements with a  $\frac{\lambda_{min}}{6}$  criterion (with  $\lambda_{min} = \frac{c}{f_{max}}$ ) to insure the convergence of the mesh.

Fig. 4 compares the SPL at listening point  $L_1$  obtained with FEM method and with the PTF approach. It shows that PTF approach converges slowly with respect to  $n_{f_{max}}$ . Fig. 5 shows the influence of the patch mesh size on the accuracy of the PTF approach. For  $n_{f_{max}} = 10$ , it appears that the error stabilizes for  $h = 2$ . Fig. 6 shows the evolution of the error in function of  $n_{f_{max}}$  and  $h$ , for two positions of the listening point.

Several observations can be made. Firstly, the calculation costs for the FEM reference solution (20k dofs) lasted about 8 minutes while the PTF method took between 2 seconds and 10 minutes depending on the parameters  $n_{f_{max}}$  and  $h$ . Fig. 4 shows that the peaks are not exactly reconstructed, which is likely due to the low absorption in the model, making them very sharp and sensitive to frequency resolution. The error is acceptable but there is disparity in the frequency range.

Additionally, the surface plot in Fig. 6 demonstrates that the error depends on the location of the listening point. When it is placed close to the

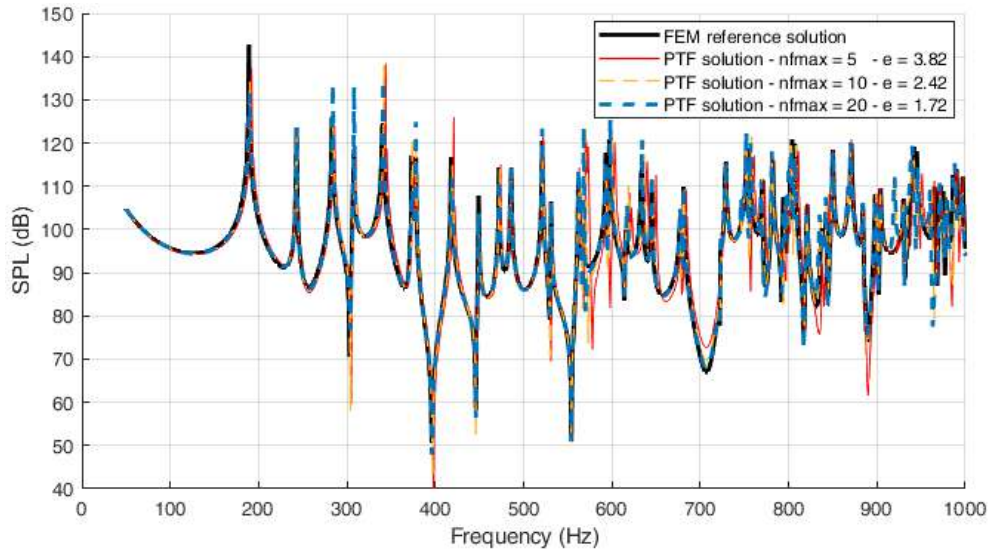


Figure 4: Influence of the modal truncation on the accuracy of the PTF approach for the calculation of the pressure at the listening point  $L_1$ . The parameter  $h$  is set to 2.

interfaces, the error increases due to artificial acoustic near field phenomenon. We can see that the error stabilizes at  $h = 2$  (a value obtained by Ouisse et al. [29]), although slightly better accuracy can be achieved with higher values (when the parameter  $n_{f_{max}}$  is above 10). Results indicate that the PTF method converges very slowly with respect to the  $n_{f_{max}}$  parameter, making the calculations time consuming when attempting to enhance the accuracy. In fact, it can be seen that modes up to 10 times the higher frequency of the study still have a significant contribution on the results. For real cases, high frequency modes will be less resonant due to the general damping, reducing their contribution. Incidentally, it would be impossible to consider modal contribution with such a high frequency for real rooms as they are much larger. Finally, a balance between accuracy and calculation costs needs to

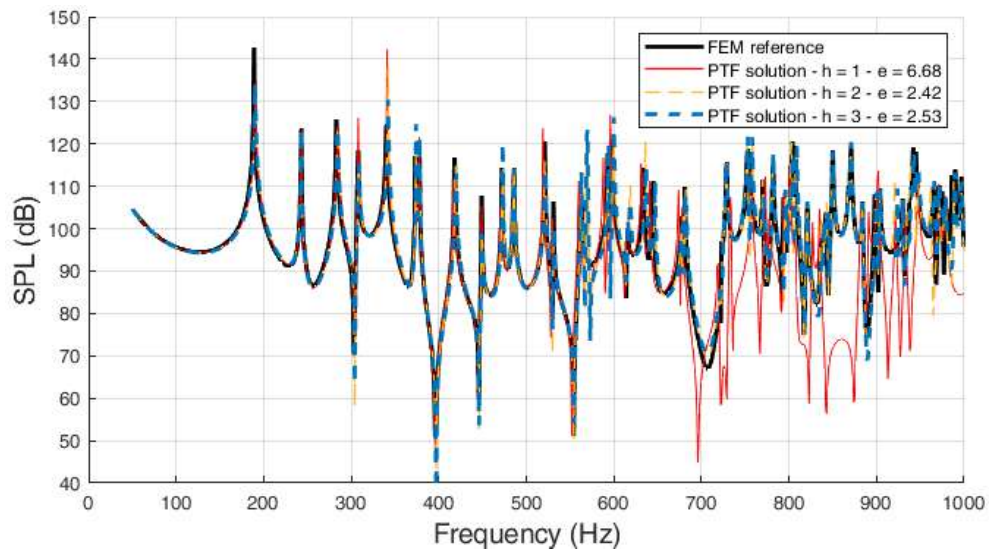


Figure 5: Influence of the patch mesh criterion  $h$  on the accuracy of the PTF approach for the calculation of the pressure at the listening point  $L_1$ . The parameter  $n_{f_{max}}$  is set to 10.

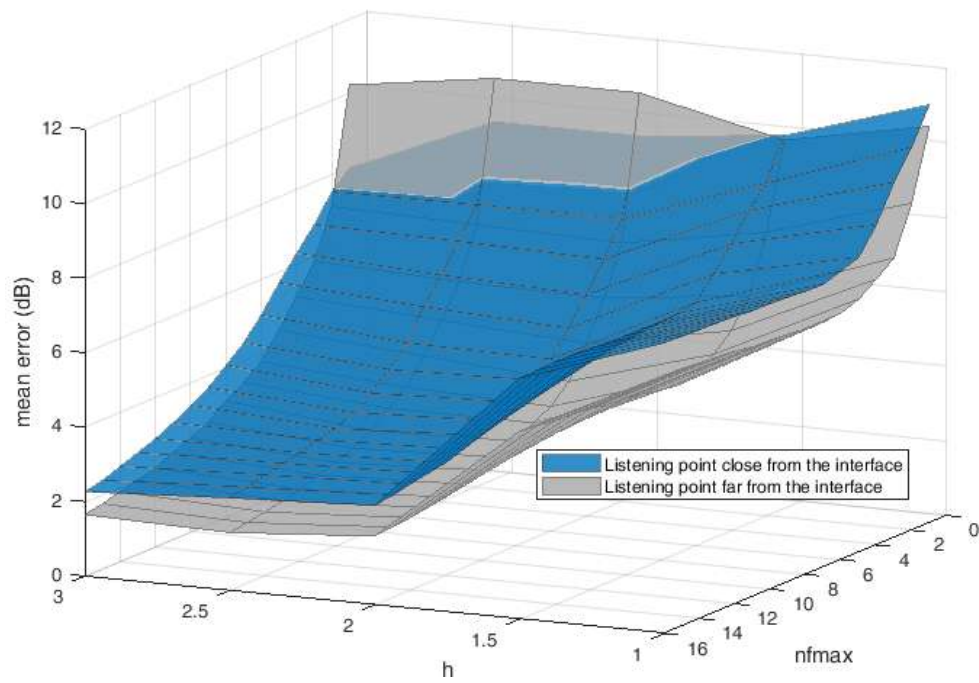


Figure 6: Error between the PTF approach and the FEM reference solution in function of  $n_{f_{max}}$  and  $h$ , for positions  $L_1$  (far from the interfaces) and  $L_2$  (close from the interfaces) of the listening point.

be found. If the PTF approach is not suitable for such a basic geometry, the next section will demonstrate that it is very efficient for geometries which cannot be solved analytically.

### 3.2.2. *Second and third cases*

The second and the third cases compare the PTF method response with a FE solution for a geometry composed of three rectangular subdomains, imitating a simple air inlet placed between two rooms (see Figs. 2 and 3b). In the second case, the central subdomain is filled with air while the air is replaced by an acoustic melamine in the third case.

Dimensions of the geometries are given in Table 2. The sizes of the rooms  $\Omega_1$  and  $\Omega_3$  are defined small enough to keep a numerical validation possible, based on the finite element method. The mesh of the whole geometry is displayed in Fig. 7. Regarding PTF calculations, the convergence criterion  $h$  is set to 2 for the patch mesh. So, in both cases, the PTF response is compared to a finite element reference solution calculated for the whole domain  $\Omega$ .

For the second configuration, all the subdomains are filled with air and PTF are obtained from an analytical modal summation (as in the previous case). For the third case, only subdomain  $\Omega_2$  varies: the air  $\Omega_2$  is replaced by an acoustic melamine. So, the PTF of subdomains  $\Omega_1$  and  $\Omega_3$  do not need to be recomputed, and the PTF of the subdomain  $\Omega_2$  are now obtained using FEM. To do this, the Johnson-Champoux-Allard model is used for the poroacoustic domain [21]. Porous parameters of the melamine are given in Table 3. Comparisons are shown in Fig. 8 and 9.

Table 2: Geometrical and physical parameters of the second system presented on Fig. 3. All lengths are in meters.

	$\Omega_1$	$\Omega_2$	$\Omega_3$
$(x ; y ; z)$	(0 ; 0 ; 0)	(1.2 ; 0.7 ; 0.644)	(1.5 ; 0 ; 0)
$(L_x ; L_y ; L_z)$	(1.2 ; 1.6 ; 1.3)	(0.3 ; 0.4 ; 0.05)	(1.5 ; 1.6 ; 1.3)
Source S	(0.2 ; 0.2 ; 0.2)		
Listening points	$L_1$ : (0.6 ; 0.8 ; 0.65), $L_2$ : (2.25 ; 0.8 ; 0.65)		
$\rho$	1.22 kg.m <sup>-3</sup>		
$c$	340 m.s <sup>-1</sup>		
$\eta$	0.02		
$(L_x ; L_y)$ Patches	6 patches of size ( $\frac{0.4}{3}$ ; 0.05)		

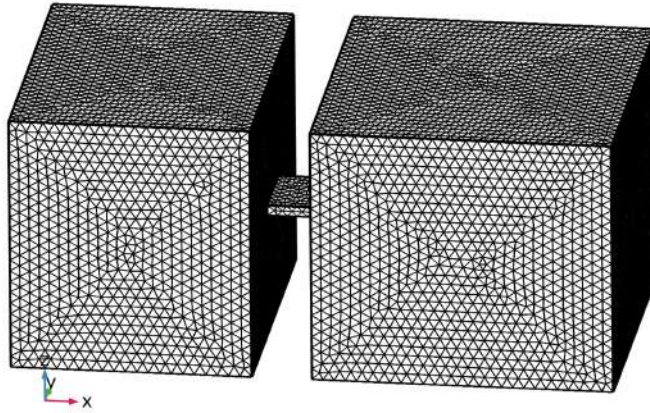


Figure 7: Finite Element mesh for the calculation of the reference solution. It has about 722 000 dofs.

Table 3: Acoustic parameters of melamine. Resistivity  $\sigma$ , porosity  $\phi$ , tortuosity  $\alpha_\infty$ , viscous length  $\Lambda$  and thermal length  $\Lambda'$  relate to the fluid phase of the porous material.

	$\sigma$	$\phi$	$\alpha_\infty$	$\Lambda$	$\Lambda'$
Units	Pa.s/m <sup>2</sup>	-	-	$\mu\text{m}$	$\mu\text{m}$
Melamine	15 300	0.96	1.02	105	205

It appears that the PTF method ensures a good prediction of the SPL at a listening point, particularly in the third case. This can be explained by the dissipation added by the presence of acoustic melamine. We can see in Fig. 9 that the melamine decreases the sound pressure level in subdomain  $\Omega_3$ . In addition, the prediction is more accurate when the listening point is in the same subdomain as the source, so in  $\Omega_1$ . Moreover, the PTF approach saves a lot of computation time for both configurations. The FEM resolution of the whole domain lasted 21 hours (it has 721 993 dofs) while the complete PTF approach lasted only 1 minute for the "air" case and about 20 minutes for the "melamine" case. The "melamine" case is longer because the PTFs of subdomain  $\Omega_2$  are computed using FEM. So, the duration of the FEM method confirms that it would be impossible to apply it to real testing rooms as their total volume is about 50 times larger, thus it would take 50 times more dofs to reach the same frequency with the same accuracy, which is totally beyond current computing resources.

However, the size of the rooms can also be a limitation for the mode expansion approach used, as the number of modes grows strongly with the

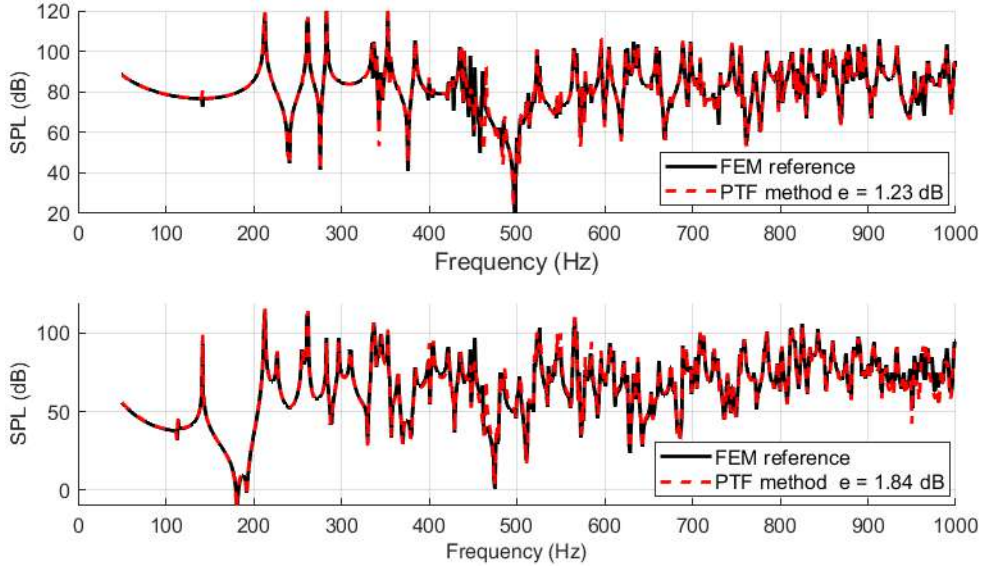


Figure 8: All the domains are filled with air. At the top: the SPL at the listening point  $L_1$ . At the bottom: the SPL at the listening point  $L_2$ .  $h = 2$ ,  $n_{f_{max}} = 6$ .

volume. The next section introduces a way to reduce the bandwidth for the calculation of modal contributions.

#### 4. Convergence acceleration of PTF computation using quasi-static correction

As the rooms increase in volume, the analytical model based on the mode expansion requires a larger number of modes to ensure convergence of the PTF which quickly becomes time consuming [36]. Thus, there is a need to speed up the calculation of the PTF using reduction methods. To this end, Aucejo et al. calculated the residual deformations on each patch and added them to their original modal basis, using a re-orthogonalization procedure [31]. This correction was applied to water cavities of relatively small

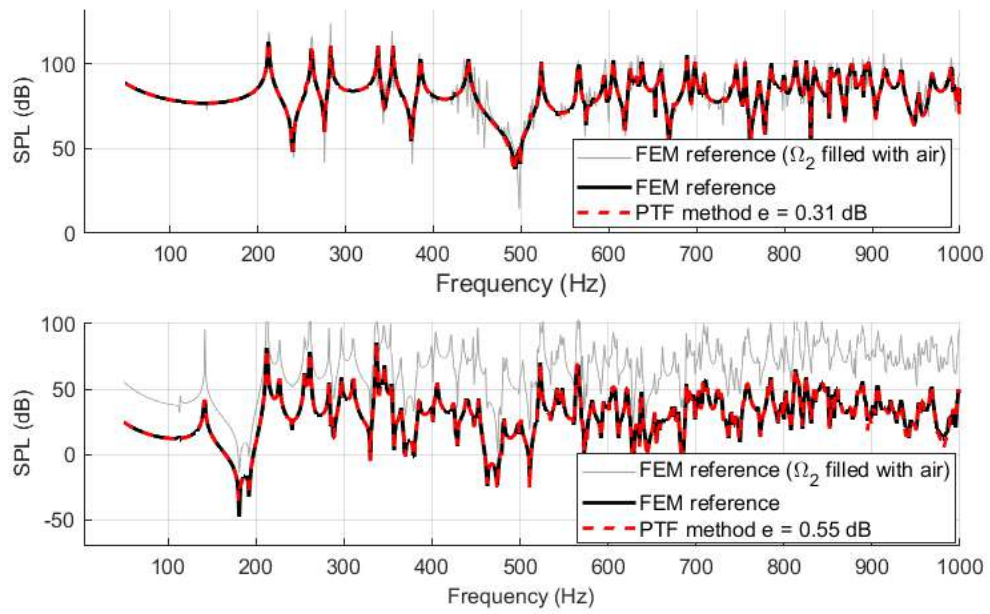


Figure 9: Subdomain  $\Omega_2$  is replaced by melamine. At the top: the SPL at the listening point  $L_1$ . At the bottom: the SPL at the listening point  $L_2$ .  $h = 2$ ,  $n_{f_{max}} = 6$ .

dimensions, containing less modes than air ones. In this section, we will illustrate how to estimate the stiffness contribution of the modes beyond the bandwidth to correct the mode approximation.

Previous results were achieved using a large number of modes in order to ensure a better convergence of the PTF quantities. The relatively small size of the considered cavities allow us to take into account modal contributions up to 6 times the upper frequency of the study, which is 6kHz. However, the volume of the real rooms used for industrial measurements is about 120 m<sup>3</sup>, which is about 50 times the volume of the largest cavity considered in the previous section. For a 3D rectangular box, the number of modes  $M$  below the frequency  $f_{mode} = n_{f_{max}} f_{max}$  can be estimated ( $f_{max}$  being the maximum frequency of the study) [28]:

$$M = \frac{4\pi V}{3} \left( \frac{f_{mode}}{c} \right)^3 + \frac{\pi S}{4} \left( \frac{f_{mode}}{c} \right)^2 + \frac{L}{8} \left( \frac{f_{mode}}{c} \right), \quad (18)$$

where  $c$  is the speed of sound,  $V$  is the room volume,  $S$  is the total area of the walls and  $L$  is the sum of all edge lengths of the room. For the cavity  $\Omega_1$  we had about 60 000 modes below 6kHz. Then if we consider the emitting room of a real acoustic laboratory, we find about 3 500 000 modes. That would make the calculation far too costly in time and memory. Thus, acceleration of the convergence is necessary in order to keep the modal approach possible for larger geometries. A quasi-static correction is defined, implemented and tested over a simple case. Benefits of this approach for convergence enhancement are shown hereunder.

#### 4.1. Definition of the implemented quasi-static correction

As we can see in Eq. (14), PTFs of any acoustic geometries have the following generic expression:

$$Z(\omega) = A(\omega) \sum_{k=1}^{\infty} \frac{\Phi_k}{(k_{eq}^2 - k_k^2) \Lambda_k}, \quad (19)$$

where  $A(\omega) = i\omega\rho_{eq}\Gamma_j$ ,  $\Phi_k$  is the product of averaged modal shapes:  $\Phi_k = \langle \phi_k^i \rangle \langle \phi_k^j \rangle$  for a PTF between two patches or  $\Phi_k = \phi_k^L \langle \phi_k^j \rangle$  for a PTF between a patch and a listening point.

This equation can be rewritten as follows:

$$Z(\omega) = A(\omega) \left( \sum_{k=1}^M \frac{\Phi_k}{(k^2 - k_k^2) \Lambda_k} + \sum_{k=M+1}^{\infty} \frac{\Phi_k}{(k^2 - k_k^2) \Lambda_k} \right), \quad (20)$$

where the left sum is the modal basis which has been kept and the right one is the truncation error.

Assuming that the natural frequencies of the omitted modes are much higher than the frequency studied:  $\omega_k \gg \omega$ , or  $k_k \gg k$ . So, the  $k^2$  term of the right summation can be neglected. The Eq. (20) simplifies:

$$Z(\omega) \approx A(\omega) \left( \sum_{k=1}^M \frac{\Phi_k}{(k^2 - k_k^2) \Lambda_k} - \sum_{k=M+1}^{\infty} \frac{\Phi_k}{k_k^2 \Lambda_k} \right). \quad (21)$$

The right sum is a constant and can be deduced from a finite element result at quasi-static frequency. For  $\omega = \omega_{qs}$ :

$$Z(\omega_{qs}) \approx A(\omega_{qs}) \left( \sum_{k=1}^M \frac{\Phi_k}{(k_{qs}^2 - k_k^2) \Lambda_k} - \sum_{k=M+1}^{\infty} \frac{\Phi_k}{k_k^2 \Lambda_k} \right) \approx Z_{FE}(\omega_{qs}), \quad (22)$$

with  $k_{qs} = \frac{\omega_{qs}}{c_{eq}}$  and  $Z_{FE}(\omega_{qs})$  the PTF obtained using the finite element method at the frequency  $\omega_{qs}$ .

Then, the infinite sum can be isolated:

$$\sum_{k=M+1}^{\infty} \frac{\Phi_k}{k_k^2 \Lambda_k} \approx \sum_{k=1}^M \frac{\Phi_k}{(k_{qs}^2 - k_k^2) \Lambda_k} - \frac{Z_{FE}(\omega_{qs})}{A(\omega_{qs})}. \quad (23)$$

Finally, the infinite sum is isolated and the Eq. (19) can be rewritten:

$$Z(\omega) \approx \frac{\omega}{\omega_{qs}} Z_{FE}(\omega_{qs}) + A(\omega) \sum_{k=1}^M \Phi_k \left( \frac{1}{(k^2 - k_k^2) \Lambda_k} - \frac{1}{(k_{qs}^2 - k_k^2) \Lambda_k} \right). \quad (24)$$

So, we get a hybrid expression of  $Z(\omega)$  calculated from an analytical mode expansion corrected with FEM. This allows for the consideration of smaller value for  $M$ , thus the summation over the number of modes is reduced and calculation time can be saved.

There is no mathematical rule for the choice of the quasi-static frequency  $\omega_{qs}$ . Empirical tests have been performed for several geometries over the entire bandwidth to identify a favorable region. We observe that the correction is more efficient when the FE calculation is computed at a frequency far from those of the eigenmodes of the considered subdomain, because the static contribution of higher modes is relatively more important away from resonances. Therefore, the following procedure has been selected for the choice of the quasistatic frequency: for each subdomain, we keep the first ten natural frequencies. Among these, we look for the two more distant ones  $\omega_a$  and  $\omega_b$ , then the calculation is made at the middle:  $\omega_{qs} = \frac{\omega_a + \omega_b}{2}$ .

#### 4.2. Validation of the quasi-static correction

The previous correction has been implemented over the second geometry presented in Fig. 2 with  $\Omega_2$  filled with air. The effect of the method is displayed in Fig. 10: the response of a FE calculation is compared with the response of the PTF calculation without and with the quasi-static correction.  $h$  and  $n_{f_{max}}$  are set to 3 for this comparison, so the modal values are calculated up to 3kHz. For the sake of clarity, a zoom is performed over the frequency range 400-1000 Hz. Note that below 400 Hz, the FE calculation and both PTF calculations give approximately the same results. We can see that the quasi-static correction drastically reduces the mean absolute error.

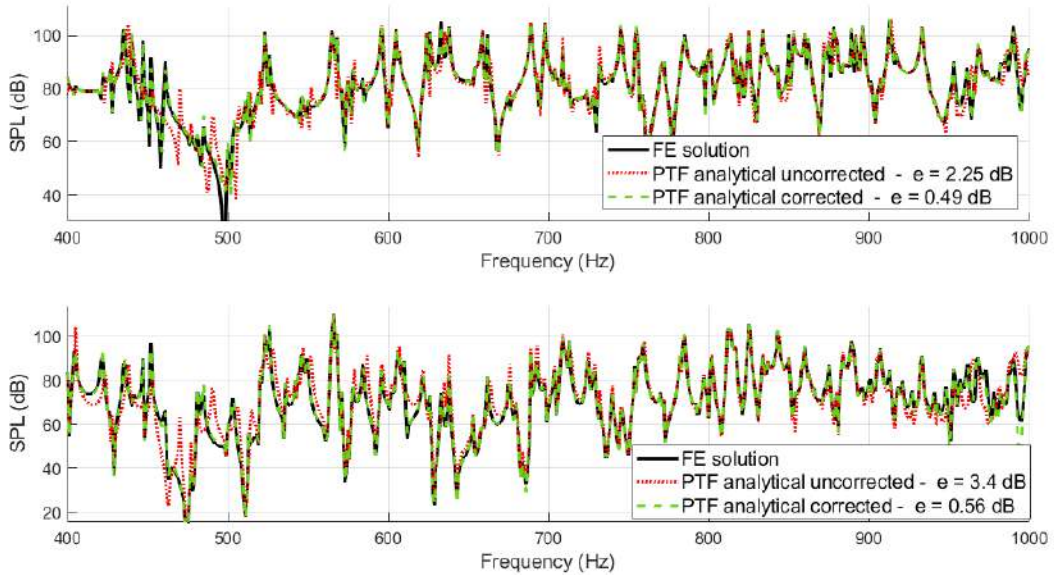


Figure 10: Comparison of the uncorrected and corrected PTF response against the FE reference. At the top: the SPL at the listening point  $L_1$ . At the bottom: the SPL at the listening point  $L_2$ .

A comparison is made between the convergence of the PTF model without

and with the quasi-static correction in Fig. 11. The mean error in dB at the listening points is calculated depending on  $n_{f_{max}}$  varying from 1 to 6. It appears that the correction allows to stay below 1 dB of mean absolute error. Moreover, we can lower  $n_{f_{max}}$  from 6 to 1 while keeping a similar error. As the number of modes is dependent on  $f^3$  (see Eq. (18)), it is equivalent to a reduction of the number of modes required by approximately 216.

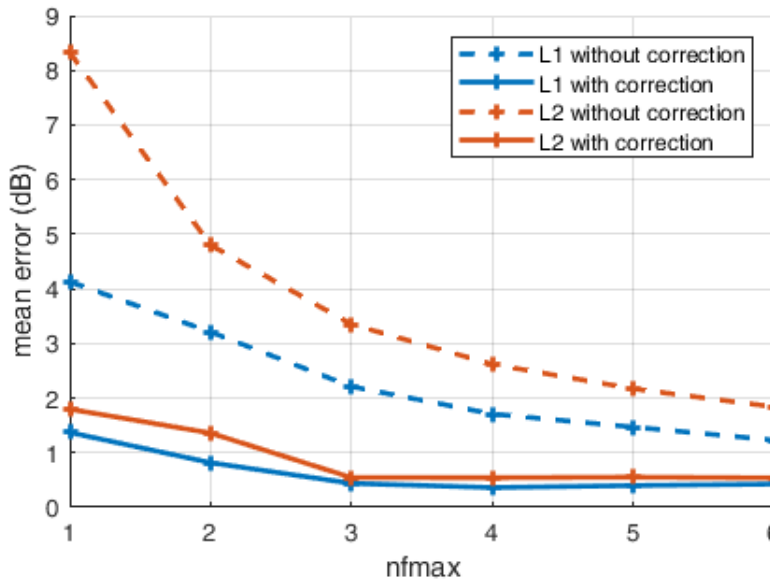


Figure 11: Convergence of the PTF model with and without the quasi-static correction, in function of the multiple of the maximum frequency kept for modal calculation.

This section demonstrated the interest of the quasi-static correction for a faster convergence of the PTF approach. As the number of modes required for a good convergence is significantly reduced, it would be possible to enlarge the size of the rectangular domains while keeping reasonable calculation costs. The next section validates a reduced model of the laboratory used for

measuring the sound transmission air inlets, opening the way for calculation with real dimensions.

## 5. Application of the PTF method on a real air inlet

The PTF method is used to model a small-scale laboratory, in order to compute the SPL at listening points located in both rooms separated by a real air inlet. This section details the reduced geometry of the real laboratory, the subdomains considered and their interfaces. It presents how the computation and the assembly of PTF sub-systems is achieved and finally compares the results with a full FEM calculation.

### 5.1. Description of the industrial case study

A 2D diagram and the 3D view of the laboratory in which the calculation of the SPL is made, is presented Fig. 12. Note that the relative shapes of the rooms are drastically reduced to allow for FEM calculation. As the emission and reception rooms have a rectangular shape, analytical solutions exist for the PTF. However, the canopy of the air inlet (where the incident surface is located) protrudes in the emission room domain. So, a fictive rectangular block is extracted from the emission room to be part of the computer aided design (CAD) domain containing the air inlet canopy, the window hole and the inner part of the air inlet. This block has to be large enough to contain various sizes of canopies (the idea is to keep the same interfaces independently of the inserted canopy), and small enough to keep the numerical computation efficient. Finally, four other rectangular blocks are created to fill the emission room.

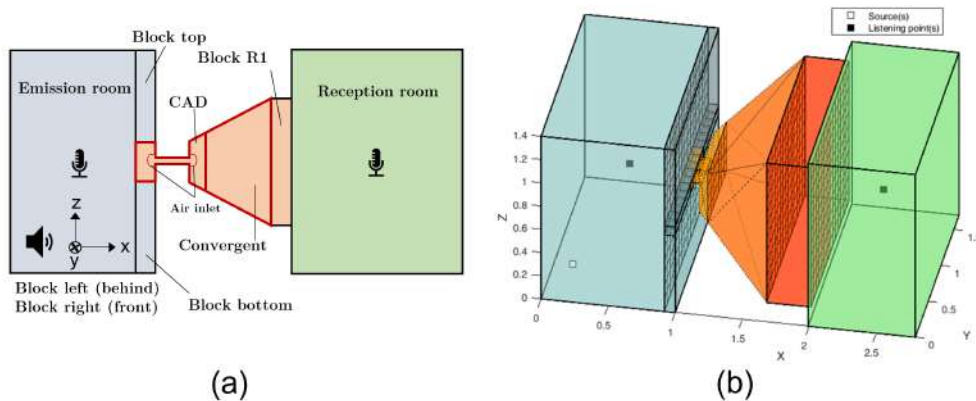


Figure 12: (a): Diagram of the industrial case (small-scale laboratory) and (b): geometry of the reduced industrial case - 9 subdomains, 16 interfaces, 569 patches. A  $\frac{\lambda}{3}$  criterion is chosen for the size of the patches.

The presented division in subdomains has two benefits. First, it allows to use an analytical model for all the rectangular blocks. On the other hand, if we change the air inlet, only the PTF of the subdomain called 'CAD' have to be recalculated. Indeed, as the interfaces remain the same, all other domains have to be computed only once. The connectivity graph presented in Fig. 13 highlights the interfaces between all the subdomains.

As displayed in Fig. 12, two listening points are placed at the center of the reduced testing rooms, and a loud speaker is placed in the emission room. All the dimensions are given in Table 4. Four configurations for the subdomain CAD are under study, as presented in Fig. 14.

The 'Convergent' is the last subdomain computed with FEM. It has about 190 000 dofs. All the results are presented in the next subsection.

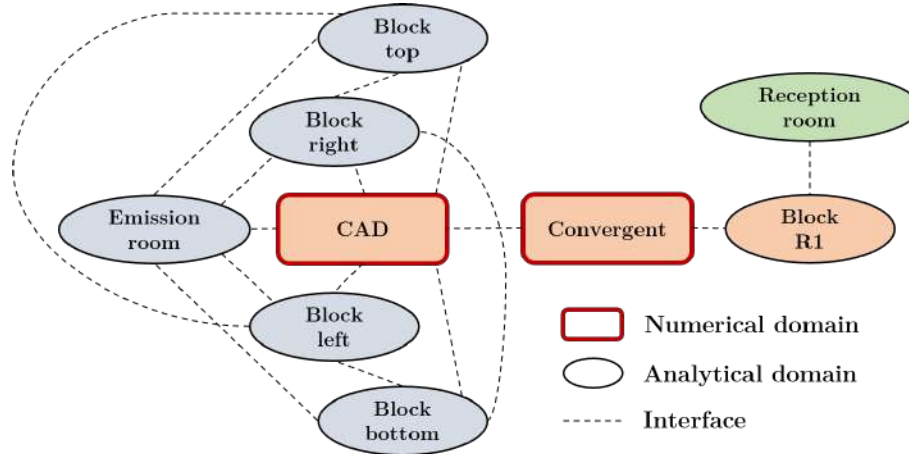


Figure 13: Subdomain connectivity graph. 9 subdomains (2 numerical, 7 analytical), 16 interfaces.

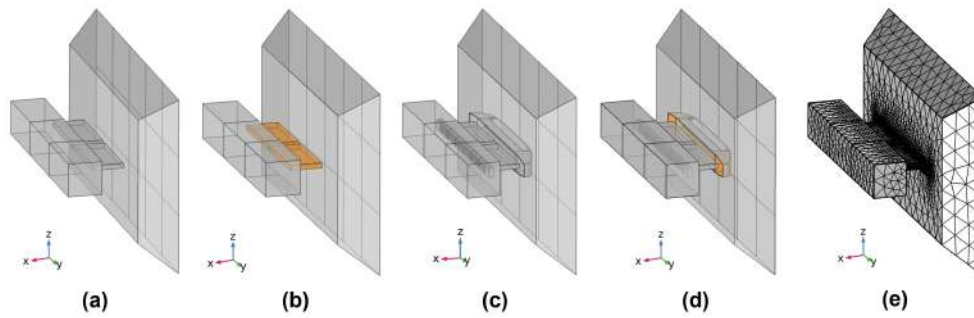


Figure 14: Four configurations are computed for the CAD domain. (a): an opening drilled in the window. (b): melamine is inserted in the opening (in orange). (c): a real air inlet is inserted without melamine foam. (d): the same air inlet with melamine foam (in orange). (e): the finite element mesh for these configurations, having about 190 000 dofs for the more complex geometry.

Table 4: Geometrical and physical parameters of the system presented on Fig. 15. All lengths are in meters.

	<b>Emission room</b>	<b>Block top</b>	<b>Block right</b>
$(x ; y ; z)$	(0 ; 0 ; 0)	(0.92 ; 0 ; 0.74)	(0.92 ; 1.1 ; 0.66)
$(L_x ; L_y ; L_z)$	(0.92 ; 1.7 ; 1.4)	(0.08 ; 1.7 ; 0.66)	(0.08 ; 0.6 ; 0.08)

<b>Block left</b>	<b>Block bottom</b>	<b>Block R1</b>	<b>Reception Room</b>
(0.92 ; 0 ; 0.66)	(0.92 ; 0 ; 0)	(1.662 ; 0.105 ; 0.1)	( 1.992 ; 0 ; 0)
(0.08 ; 0.6 ; 0.08)	(0.08 ; 1.7 ; 0.66)	(0.33 ; 1.49 ; 1.2)	(0.8 ; 1.7 ; 1.4)

<b>Source S</b>	(0.2 ; 0.2 ; 0.2)
<b>Listening points</b>	L <sub>1</sub> : (0.5 ; 0.85 ; 0.7) and L <sub>2</sub> : (2.392 ; 0.85 ; 0.7)
$\rho$	1.22 kg.m <sup>-3</sup>
$c$	340 m.s <sup>-1</sup>
$\eta$	0.02
<b>Patches</b>	569 patches of maximum size 0.11 m

## 5.2. Implementation of the computation and assembly of PTF subsystems

The relative complexity of the industrial case led to the development of an application dedicated to the creation of the geometries, the detection of the interfaces, the creation of the patches and all the acoustic calculations based on the PTF method. The program is structured around the following steps:

1. Sizing and positioning of all the subdomains, sources and listening points;
2. Definition of the frequency range, the maximum size of the patches, the maximum frequency for the modal bases;
3. Calculation of the natural frequencies and the associated modal mass and damping for each rectangular subdomain;
4. Detection of the coupling surfaces between each subdomain, definition of a list of neighboring subdomains for each subdomain;
5. Definition of the patches;
6. Calculation of the averaged mode shapes on each patch, and the mode shape at source points and listening points for each rectangular subdomain;
7. Loading of the pre-calculated PTF matrices of FE domains;
8. Initialization of the general PTF block matrix;
9. Calculation of quasi-static corrections for each analytical domain;
10. Starting the frequency loop: calculation of all the patch transfer functions, resolution of the matrix system (velocity on the patches) and calculation of the pressure at the listening points;
11. Save the PTF matrices for future calculations;

## 12. Post-processing and display.

### 5.3. FEM validation

In order to validate the implementation, the same geometry is computed using FEM. A comparison of the meshes used for the PTF approach and the full FEM approach is displayed in Fig. 15.

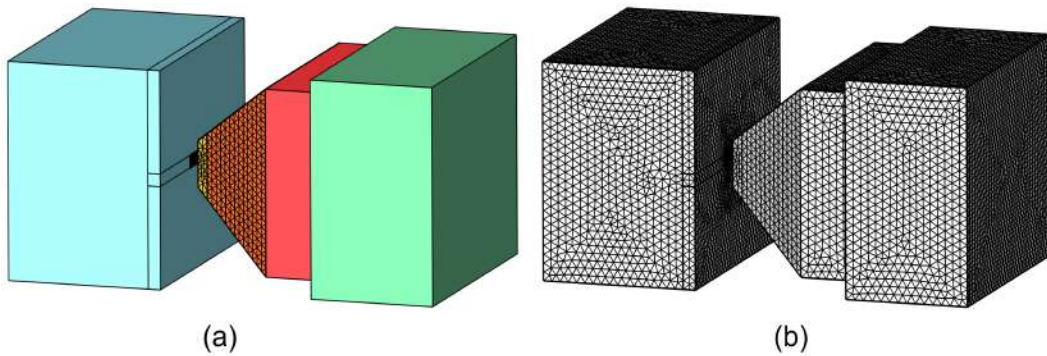


Figure 15: (a): Meshed domains for the PTF approach. CAD subdomain has 32 000 dofs, convergent subdomain has 61 000 dofs. (b): mesh of the complete domain for the calculation of FE reference (about 900 000 dofs).

### 5.4. Results

Results of the reduced industrial case are presented for the four configurations. Parameter  $n_{f_{max}}$  is set to 3, and the quasi-static correction is used for all the rectangular subdomains. Parameter  $h$  is set to 3. It provides better results in this complex configuration having lots of subdomains and mixing analytical and numerical PTF matrices. Other tests (not presented here) with  $h = 2$  have shown that the error is cumulative and grows with the number of subdomains.

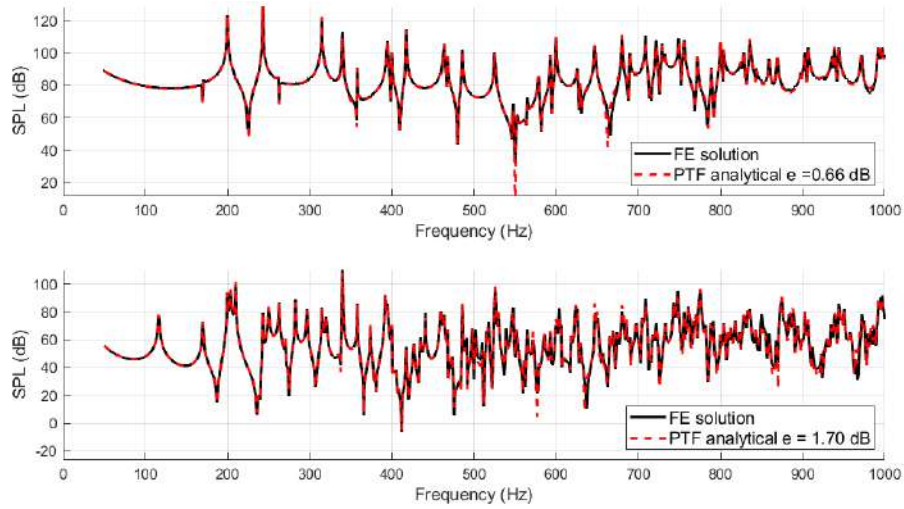


Figure 16: First case: The CAD domain only contains the opening filled with air. At the top: the SPL at listening point  $L_1$ . At the bottom: the SPL at listening point  $L_2$ .

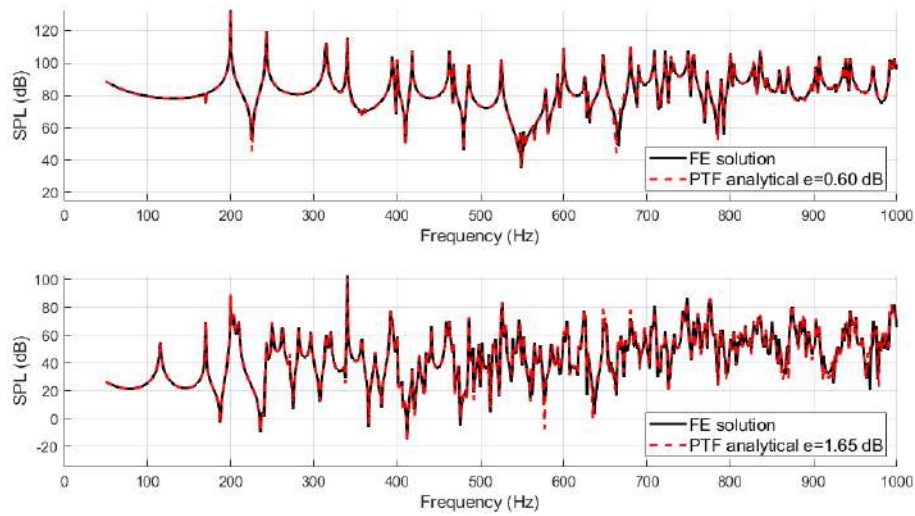


Figure 17: Second case: The CAD domain only contains the opening filled with melamine. At the top: the SPL at listening point  $L_1$ . At the bottom: the SPL at listening point  $L_2$ .

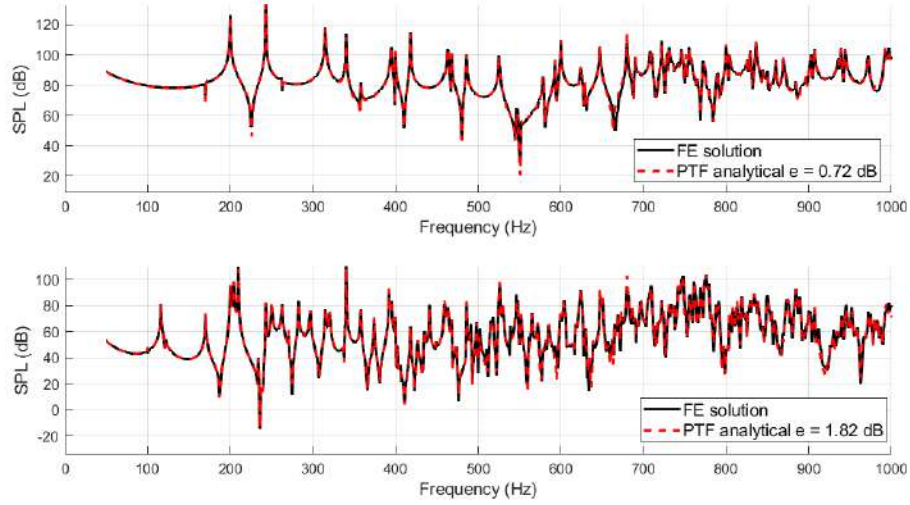


Figure 18: Third case: The CAD domain contains the air inlet without melamine foam. At the top: the SPL at listening point  $L_1$ . At the bottom: the SPL at listening point  $L_2$ .

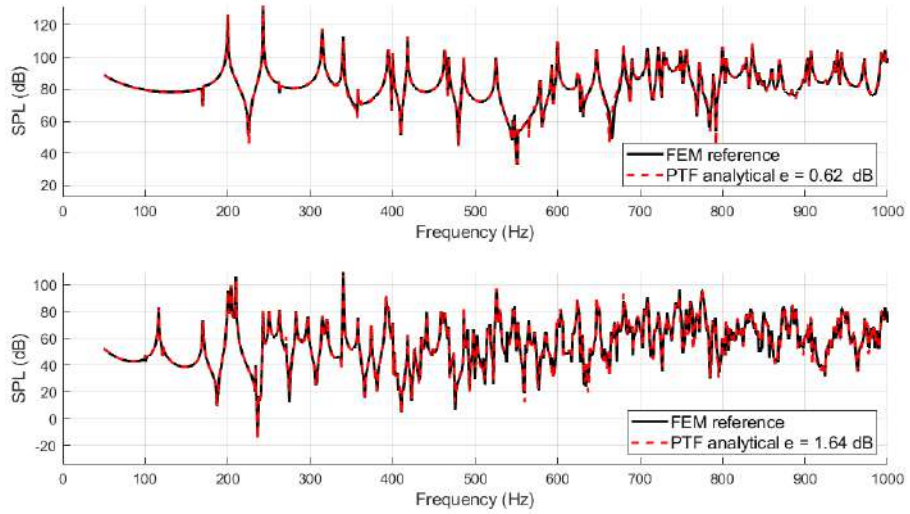


Figure 19: Fourth case: The CAD domain contains the air inlet with melamine foam. At the top: the SPL at listening point  $L_1$ . At the bottom: the SPL at listening point  $L_2$ .

Figures 16, 17, 18 and 19 show that differences between the configurations are hardly noticeable because of the low dissipation inducing strong resonances. In all cases, the mean error between the PTF response and the FEM reference is reasonably low which validates the implementation. Table 5 shows the duration of all the calculations.

Table 5: Detailed calculation costs for FEM and PTF methods. PTF analytical and quasi-static correction lines concerns the calculation of the PTF of all rectangular subsystems.

<b>Case considered</b>	<b>1</b>	<b>2</b>	<b>3</b>	<b>4</b>
<b>FEM</b>	14h 20min	14h 20min	19h 10min	19h 10min
<b>PTF analytical</b>	3min	-	-	-
<b>Quasi-static correction</b>	25min	-	-	-
<b>PTF of Convergent</b>	30h	-	-	-
<b>PTF of CAD</b>	12h 20min	12h 20min	17h 30min	17h 30min
<b>PTF resolution</b>	15s	15s	15s	15s
<b>PTF total</b>	42h 50min	12h20min	17h 30min	17h 30min

Table 5 states that the PTF approach and the FEM reference took approximatively the same time to compute, except for the first case (43 hours) as it includes the calculation of the PTF of all the rectangular domains plus the Convergent subsystem. As these subsystems and interfaces remain the same between configurations, their PTF are simply reused for the other cases, this is one of the interests of this approach. We are here considering a reduced case: the volume of the real testing rooms is about 50 times larger (as well as the number of dofs), making the use of FEM almost unfeasible

on standard computers. Conversely, with the PTF approach, we will first need to calculate the PTF of the uncoupled rectangular subsystems which should take a few hours, because the number of modes increases along with frequency. Once these PTFs are calculated, the total duration of all the other cases will not change as it depends only on the duration of the PTF of CAD subsystem calculation. Note that the PTF resolution will last longer because of the increasing number of patches. However, it remains negligible compared to the total duration. The duration of quasi-static correction should not vary a lot since it is computed around the first eigenmodes of the rectangular subsystems. Preliminary calculations on real size geometries required about 40 hours to compute the PTF matrices of all the rectangular subdomains due to a high number of patches (around 2000) and the multiplication of eigenmodes. However, the duration of PTF resolution remains below 10 minutes. Finally, these results open the way for calculations on real testing rooms.

## 6. Conclusion

A model of an air inlet coupled with testing rooms was presented, utilizing the PTF method to calculate the SPL at a listening point generated by a monopole source. The model included analytical mode expansion for rectangular cavities and used FEM for more complex geometries. A convergence acceleration was successfully implemented for the analytical calculations. It allows to reduce by half the maximum frequency for the modal summation, making calculations on large testing rooms possible. Melamine foams inside the air inlets are also considered using an equivalent fluid model.

The results showed the accuracy of the PTF approach, as the results

were similar to the FEM model for all the geometries considered. It was also demonstrated that the calculation of PTF in subdomains is a fast process, and has the advantage of remaining nearly the same with larger testing rooms where FEM is no longer applicable. This demonstrates again the considerable interest of this approach. Upcoming developments will extend the study to a model with real dimensions and compare predicted  $D_{n,e}$  with measured ones for several air inlets. It will be necessary to calibrate the testing room responses using measurements made in a specific laboratory. To ensure the accuracy, dissipative interfaces will be plugged into several locations on the walls of the testing room to replicate the behavior of a real testing facility.

### **Acknowledgements**

The authors would like to express their thanks to CODIFAB (Comité professionnel de développement des industries françaises de l'ameublement et du bois) for its financial support.

### **References**

- [1] European Environment Agency. Environmental noise in europe, 2020. *Publications Office*, 2020.
- [2] *NF EN ISO 10140 : Acoustique - Mesurage en laboratoire de l'isolation acoustique des éléments de construction*, 2013.
- [3] *NF EN ISO 717 : Acoustique - Évaluation de l'isolement acoustique des immeubles et des éléments de construction*, 2013.

- [4] T. Kihlman and A. C. Nilsson. The effects of some laboratory designs and mounting conditions on reduction index measurements. *Journal of Sound and Vibration*, 24:349–364, 1972.
- [5] T. Bravo and S. J. Elliott. Variability of low frequency sound transmission measurements. *The Journal of the Acoustical Society of America*, 115:2986–2997, 2004.
- [6] J. Mahn and J. Pearse. The uncertainty of the proposed single number ratings for airborne sound insulation. *Building Acoustics*, 19:145–172, 2012.
- [7] C. Scrosati, Scamoni F., Bassanino M., M. Mussin, and G. Zambon. Uncertainty analysis by a round robin test of field measurements of sound insulation in buildings: Single numbers and low frequency bands evaluation - airborne sound insulation. *Noise Control Engineering journal*, 61:291–306, 2013.
- [8] M. Machimbarrena, C. R. A. Monteiro, S. Pedersoli, R. Johansson, and S. Smith. Uncertainty determination of in situ airborne sound insulation measurements. *Applied Acoustics*, 89:199–210, 2014.
- [9] N. Garg and S. Maji. On analyzing the correlations and implications of single-number quantities for rating airborne sound insulation in the frequency range 50 hz to 5 khz. *Building Acoustics*, 22:29–44, 2015.
- [10] H. K. Park and H. Kim. Acoustic insulation performance of improved airtight windows. *Journal of Computational Acoustics*, 176:1550020, 2016.

- [11] C. Soussi, M. Aucejo, W. Larbi, and J.-F. Deü. Numerical analyses of the sound transmission at low frequencies of a calibrated insulating glazing unit. *Applied Acoustics*, 179:108065, 2021.
- [12] X. Yu, S.-K. Lau, L. Cheng, and F. Cui. A numerical investigation on the sound insulation of ventilation windows. *Applied Acoustics*, 117:113–121, 2017.
- [13] H. Huang, X. Qiu, and J. Kang. Active noise attenuation in ventilation windows. *The Journal of the Acoustical Society of America*, 130:176–188, 2011.
- [14] P. Jean. Modeling of sound transmission through air inlets. In Proceedings of 16th International Congress on Sound and Vibration, 2009.
- [15] P. Jean, C. Guigou-Carter, and R. Foret. Using finite elements to model porous materials in buildings. In Proceedings of 39th International Congress on Noise Control Engineering, 2010.
- [16] J. Puig, J.-F. Deü, W. Larbi, and M. Aucejo. Numerical simulation of air inlet sound insulation. In Proceedings of 50th International Congress and Expo on Noise Control Engineering, 2021.
- [17] G. M. L. Gladwell. A finite element method for acoustics (acoustic problems formulated and solved by finite element method of variational calculus, using both force and displacement procedures). In the 5th International Congress on Acoustics, Volume 7, 1965.
- [18] O. Dazel, C.-H. Sgard, and N. Atalla. An extension of complex modes for

- the resolution of finite-element poroelastic problems. *Journal of Sound and Vibration*, pages 253(2) :421–445, 2002.
- [19] L. Gaul, M. Kögl, and M. Wagner. *Boundary Element Methods for Engineers and Scientists*. Springer Berlin, Heidelberg, 1st edition, 2003.
- [20] K. Verdière, R. Panneton, S. Elkoun, T. Dupont, and P. Leclaire. Transfer matrix method applied to the parallel assembly of sound absorbing materials. *Journal of the Acoustical Society of America*, pages 134(6) :4648–4658, 2013.
- [21] J. Allard. *Propagation of Sound in Porous Media: Modelling Sound Absorbing Materials*. Wiley, 2nd edition, 1993.
- [22] Q. Serra, M. Ichchou, and J.-F. Deü. On the use of transfer approaches to predict the vibroacoustic response of poroelastic media. *Journal of Computational Acoustics*, 24 (02):1550020, 2016.
- [23] Allan D. Pierce. *Acoustics - An Introduction to Its Physical Principles and Applications*. Springer Cham, 3rd edition, 2019.
- [24] T. Lafont, N. Totaro, and A. Le Bot. Review of statistical energy analysis hypotheses in vibroacoustics. *Processings of the Royal society A*, 470 (2162):20130515 (20 p.), 2014.
- [25] Richard H. Lyon and Richard G. DeJong. *Theory and Application of Statistical Energy Analysis*. Elsevier, 2nd edition, 1995.
- [26] R. S Langley. A wave intensity technique for the analysis oh high fre-

- quency vibrations. *Journal of Sound and vibrations*, 159(3):486–502, 1994.
- [27] D. J. Nefske and S. H. Sung. Power flow finite element analysis of dynamic systems : basic theory and application to beams. *Journal of Vibration and Acoustics - Transactions of ASME*, 111:97–100, 1989.
- [28] H. Kuttruff. *Room Acoustics*. CRC Press, 6th edition, 2016.
- [29] M. Ouisse, L. Maxit, C. Cacciolati, and J.-L. Guyader. Patch transfer functions as a tool to couple linear acoustic problems. *Journal of Vibration and Acoustics*, 127:458–466, 2005.
- [30] J.-D. Chazot and J.-L. Guyader. Prediction of transmission loss of double panels with a patch-mobility method. *J. Acoust. Soc. Am*, 121(1):267–278, 2007.
- [31] M. Aucejo, L. Maxit, N. Totaro, and J.-L. Guyader. Convergence acceleration using the residual shape technique when solving structure-acoustic coupling with the patch transfer functions method. *Computers & Structures*, 88 (11 - 12):728–736, 2010.
- [32] M. Grialou, N. Totaro, J.-L. Guyader, and A. Bocquillet. Characterization of surface impedance of vibro-acoustic subdomains with experimental measurements. *Journal of Sound and Vibration*, 460:114876, 2019.
- [33] A. Preumont. *Vibration Control of Active Structures, An Introduction*. Springer International Publishing, 4th edition, 2018.

- [34] G. Veronesi, C. Albert, E. Nijman, and J. et al. Rejlek. Patch transfer function approach for analysis of coupled vibro-acoustic problems involving porous materials. 2014.
- [35] D.T. Blackstock. *Fundamentals of Physical Acoustics*. John Wiley & Sons, 1st edition, 2000.
- [36] M. Tournour and N. Atalla. Pseudostatic corrections for the forced vibroacoustic response of a structure-cavity system. *The journal of the Acoustical Society of America*, 107:2379–2386, 2000.